DYNAMIC BIOSCAFFOLDS

Bioactive scaffolds with enhanced supramolecular motion promote recovery from spinal cord injury

Z. Álvarez^{1,2}, A. N. Kolberg-Edelbrock^{1,3}, I. R. Sasselli^{1,4}†, J. A. Ortega^{1,5}, R. Qiu^{1,4}, Z. Syrgiannis^{1,4}, P. A. Mirau⁶, F. Chen¹, S. M. Chin^{1,4}, S. Weigand⁷, E. Kiskinis^{1,5}, S. I. Stupp^{1,2,3,4,8}*

The signaling of cells by scaffolds of synthetic molecules that mimic proteins is known to be effective in the regeneration of tissues. Here, we describe peptide amphiphile supramolecular polymers containing two distinct signals and test them in a mouse model of severe spinal cord injury. One signal activates the transmembrane receptor $\beta 1$ -integrin and a second one activates the basic fibroblast growth factor 2 receptor. By mutating the peptide sequence of the amphiphilic monomers in nonbioactive domains, we intensified the motions of molecules within scaffold fibrils. This resulted in notable differences in vascular growth, axonal regeneration, myelination, survival of motor neurons, reduced gliosis, and functional recovery. We hypothesize that the signaling of cells by ensembles of molecules could be optimized by tuning their internal motions.

harmacological signaling of cells usually proceeds through the strong binding of small organic molecules to proteins that activate or inhibit particular responses. An emerging signaling strategy is to use nanostructures that target specific cells to deliver a therapeutic cargo or materials functioning as bioactive scaffolds in the extracellular space. Cell-signaling materials that trigger the regeneration of tissues mimic the fibrillar components of natural extracellular matrices (ECMs) (1). Mechanobiology has been an important part of the science behind this idea on the basis of the discovery that stiffness and viscoelasticity of materials can mediate multiple aspects of cell behavior (2).

Less-developed aspects of this field are the molecular design of materials bearing signals for receptors and the connections between such signals and the motions of molecules within artificial scaffolds. Bioactive signals have been incorporated into covalent polymers (3) and more recently in supramolecular polymers (4). A commonly investigated signal has been the peptide RGDS, present in

extracellular fibrils, such as fibronectin, that promote cellular adhesion. Supramolecular polymers, which form by noncovalent association among monomers, have potential advantages for regenerative signaling because of the easy tunability of signal density, their ability to architecturally mimic the high-persistence length of natural ECM fibrils, and their rapid biodegradation after they serve their function (5).

Here, we report a supramolecular scaffold of nanoscale fibrils that integrates two different orthogonal biological signals-the laminin signal IKVAV known to promote differentiation of neural stem cells into neurons and to extend axons (1) and the fibroblast growth factor 2 (FGF-2) mimetic peptide YRSRKYSSWYVALKR, which activates the receptor FGFR1 to promote cell proliferation and survival (6). The two signals were placed at the termini of two different peptides with alkyl tails, known as peptide amphiphiles (PAs), that copolymerize noncovalently in aqueous media to form supramolecular fibrils. It was previously shown that the IKVAV signal on PA supramolecular polymers could restore partial function after a mild compression injury in a mouse model of spinal cord injury (SCI) (7). Fibril-forming PA molecules that display biological signals at one terminus contain peptide domains between the bioactive moiety and the alkyl tail that can be modified to tune mechanical properties (8, 9).

We therefore investigated different domains that alter the physical properties of a potential scaffold therapy to restore functional recovery in vivo after hind limb paralysis in a murine model of severe SCI. The development of SCI therapies that avoid permanent paralysis in humans after traumatic injuries remains a major challenge given the inability of damaged axons to regenerate in the adult central nervous system (CNS) (10, 11). We found that keeping both biological signals at the same

density while slightly mutating the tetrapeptide sequence of these domains could markedly change the biological responses of cells in vitro as well as the functional recovery from SCI in mice in vivo.

Supramolecular polymer synthesis and characterization

To investigate nanofiber-shaped supramolecular polymers with different physical properties that display the same two signals, we synthesized a library of different IKVAV PAs in which the tetrapeptide domain controlling physical behavior has different sequences of the amino acids V, A, and G (IKVAV PA1 to PA8) (see Fig. 1A, fig. S1, and table S1 for the list of PAs used and their peptide sequences). These amino acids were selected because they affect the propensity of molecules within the fibrils to form β sheets, which have high intermolecular cohesion as a result of their hydrogen bond density. These interactions in turn result in suppressed mobility of PA molecules within the fibril. For example, V₂A₂ (PA1) has a high propensity to form β sheet structure because of its valine content, whereas A₂G₂ (PA2) is potentially a less-ordered segment without secondary structure (Fig. 1A). The rest of the sequences were selected as potential candidates for an intermediate level of motion. All IKVAV PAs utilized the sequence E₄G, which spaces this segment from the bioactive signal and provides high solubility in water (12).

Cryo-transmission electron microscopy (crvo-TEM) revealed that all IKVAV PAs formed nanofibers after supramolecular polymerization in water (Fig. 1B). Furthermore, synchrotron solution small-angle x-ray scattering (SAXS) confirmed the formation of filaments, revealing a slope in the range of -1 to -1.7 in the Guinier region except for that of PA5, which suggests a mixture of filaments and spherical micelles (slope = -0.2) (Fig. 1D). We also compared the physical behavior of the various assemblies in the library using coarse-grained molecular dynamic (CG-MD) simulations using the MARTINI force field (13) (fig. S2 and supplementary materials). These simulations predicted that molecules within the various IKVAV PA fibers had different degrees of internal dynamics (Fig. 1B). Differences in the ability of the molecules to change positions internally over appreciable distances (on the order of nanometers) were suggested by the simulations, which yielded values of the parameter defined as the root mean square fluctuation (RMSF). which is a measure of the average displacement of a PA molecule during the last 5 µs of the simulation (Fig. 1C). These simulations indicate that molecules in PA2 fibers do in fact have a high degree of internal motion, including PA5, which only contains G residues. Wideangle x-ray scattering (WAXS) also revealed the

*Corresponding author. Email: s-stupp@northwestern.edu †Present address: Center for Cooperative Research in Biomaterials (CIC biomaGUNE), Basque Research and Technology Alliance (BRTA), Donostia, San Sebastián, 20014, Spain.

¹Simpson Querrey Institute for BioNanotechnology, Northwestern University, Chicago, IL 60611, USA. ²Department of Medicine, Northwestern University, Chicago, IL 60611, USA. ³Department of Biomedical Engineering, Northwestern University, Evanston, IL 60208, USA. ⁴Department of Chemistry, Northwestern University, Evanston, IL 60208, USA. ⁵The Ken & Ruth Davee Department of Neurology, Department of Physiology, Feinberg School of Medicine, Northwestern University, Chicago, IL 60611, USA. ⁶Materials and Manufacturing Directorate, Nanostructured and Biological Materials Branch, Air Force Research Laboratories, Wright-Patterson AFB, OH 45433, USA. ⁷DuPont-Northwestern-Dow Collaborative Access Team Synchrotron Research Center, Northwestern University, DND-CAT, Argonne, IL 60439, USA. ⁸Department of Materials Science and Engineering, Northwestern University, Evanston, IL 60208, USA.

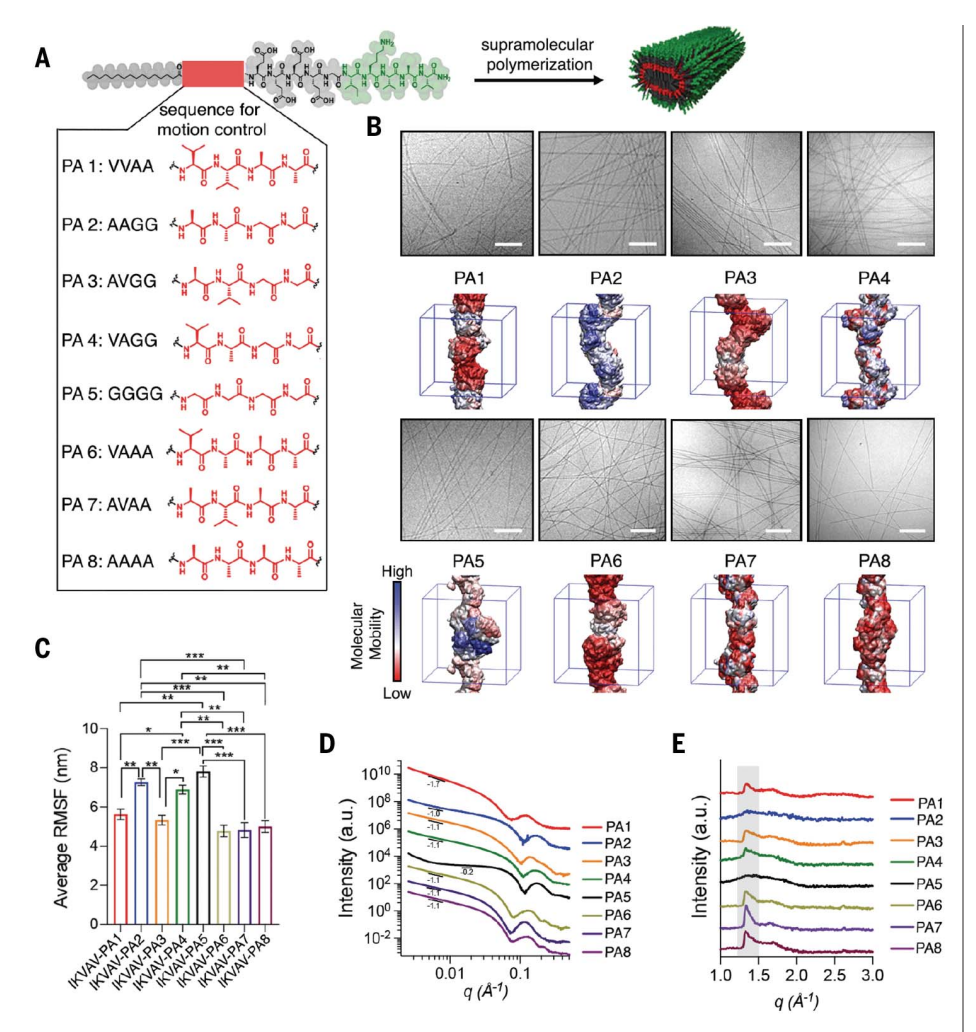


Fig. 1. Library of investigated IKVAV PA molecules. (**A**) Specific chemical structures of IKVAV PA molecules used and molecular graphics representation of a supramolecular nanofiber displaying the IKVAV bioactive signal. (**B**) Cryo-TEM micrographs of IKVAV PAs in the library and their corresponding color-coded representations of RMSF values for single IKVAV PA filaments. (**C**) Bar graphs of the average RMSF values of the different IKVAV PA molecules. Error bars correspond to three independent simulations. *P < 0.05; **P < 0.01; ***P < 0.001; one-way analysis of variance (ANOVA) with Bonferroni. (**D** and **E**) SAXS patterns (D) and WAXS profiles (E) of the different IKVAV PA nanofibers. The scattering intensities were offset vertically for clarity; the Bragg peak corresponding to the β sheet spacing around 1.35 Å is framed in a gray box. a.u., arbitrary units. Scale bars, 200 nm.

presence of internal order (β sheet Bragg peak with a d-spacing of 4.65 Å) in all the IKVAV PAs except for those with high RMSF values (PA2 and PA5) (Fig. 1E).

To probe differences in dynamics among the IKVAV PAs, we performed fluorescence depolarization (FD) measurements by encapsulating 1,6-diphenyl-1,3,5-hexatriene (DPH) within PA nanofibers to measure the microviscosity of the inner hydrophobic core. As expected, PA2 and PA5 had the lowest anisotropy values (0.21 and 0.18, respectively), indicating that they formed the most dynamic supramolecular assemblies; PA4 had intermediate dynamics (0.30); and the remaining

PAs had less-intense supramolecular motion (0.40 to 0.37) (Fig. 2A). We also measured molecular dynamics in the IKVAV epitope using transverse-relaxation nuclear magnetic resonance (T2-NMR) spectroscopy. These experiments obtained the relaxation rate for the methylene protons attached to the ϵ carbon (H $_\epsilon$) of the K residue in the IKVAV sequence [observed at 2.69 to 2.99 parts per million (ppm)] (figs. S3 to S10 and table S2). IKVAV PA1 showed the highest relaxation rate (a low degree of motion), whereas IKVAV PA2 and PA5 had the lowest relaxation rates in the IKVAV PA library ($^1\text{H-R}_2 = 2.7 \pm 0.1$ and 2.6 \pm 0.003 s $^{-1}$, respectively, consistent with greater

motion) (Fig. 2B, figs. S3 to S10, and table S2). Consistent with FD results, IKVAV PA4 revealed an intermediate level of supramolecular motion, between that of PA1 and PA2 (or PA5). Collectively, the simulations as well as the FD, WAXS, and T2-NMR measurements are consistent with three levels of supramolecular motion in the library of molecules investigated.

Supramolecular motion and in vitro bioactivity

We performed in vitro experiments to determine whether the IKVAV signal was equally bioactive in the library of IKVAV PAs. To establish the bioactivity of IKVAV PAs, neural progenitor cells derived from human embryonic stem cells [human neural progenitor cells (hNPCs)] were treated either with the different IKVAV PA fibers in solution or the recombinant protein laminin (Fig. 2C). PA filaments associate closely with cells and can activate receptors when their surfaces display signals (14).

We first investigated the activation of the transmembrane receptor β1-INTEGRIN (ITGB1), known to be expressed in the presence of IKVAV PAs and laminin (15-17), using the active formspecific antibody HUTS4 and also verified activation of the receptor's intracellular signaling pathway. Fluorescence confocal microscopy and Western blot (WB) analysis showed that IKVAV PA2 and PA5 induced significantly higher concentrations of active ITGB1 and the downstream effectors integrin-linked kinase (ILK) and phospho-focal adhesion kinase (p-FAK) relative to the rest of the IKVAV PAs, the IKVAV peptide, and laminin or ornithine coatings as controls (Fig. 2, D and E, and figs. S11 and S12). We observed an intermediate level of activation with PA4 that correlated with its intermediate supramolecular motion relative to the rest of the PAs in the library. As expected, PAs displaying the VVIAK scrambled sequence resulted in minimal cellular activation of ITGB1 (figs. S12 and S13). Furthermore, pretreatment with an ITGB1 antibody blocked the attachment of hNPCs on all IKVAV PAs, which suggests that an IKVAV-ITGB1 interaction mediated this process (fig. S14).

Although hNPCs up-regulated the neuronal form of β -TUBULIN (TUJ-1⁺) when treated with IKVAV PAs, this induction (which reflects neuronal differentiation commitment) was higher for IKVAV PA2 and PA5 (20.5 ± 1% and 20.7 ± 1.2%, respectively), the two most dynamic supramolecular fibrils (Fig. 2, F to H, and fig. S15). The other IKVAV PAs, with the exception of IKVAV PA4 that showed an intermediate neuronal differentiation commitment (PA4: 14 ± 1.2%), had a lower percentage of induction of TUJ-1⁺ neuronal cells (PA1: 8.2 ± 0.7%; PA3: 7.5 ± 0.6%; PA6: 7.9 ± 1.3%; PA7: 7.4 ± 0.6%; and PA8: 7.5 ± 0.5%). By using

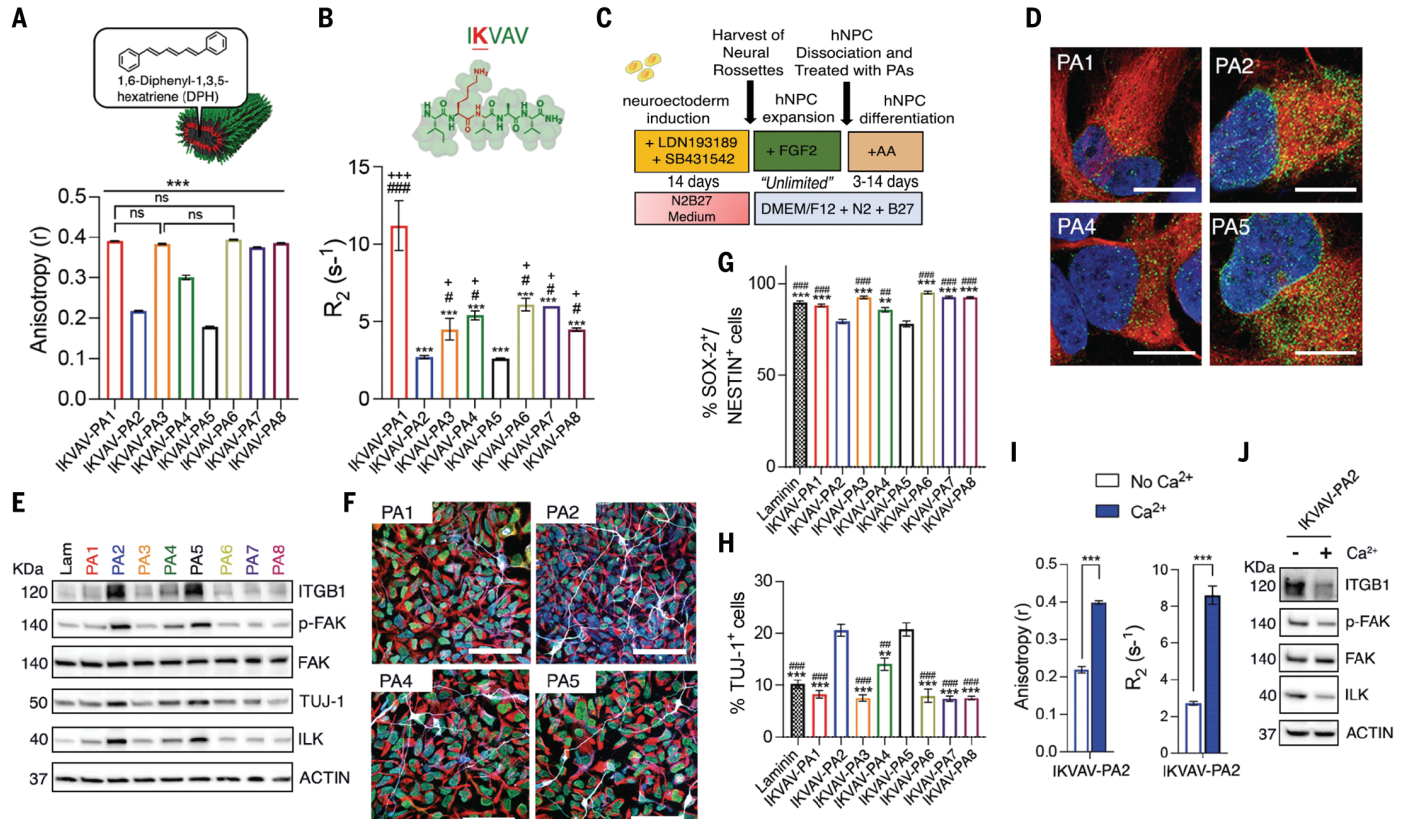


Fig. 2. Effect of supramolecular motion on hNPCs signaling in vitro.

(A) (Top) Molecular graphics representation of an IKVAV PA nanofiber indicating the chemical structure and location of DPH used as a probe in fluorescence depolarization measurements. (Bottom) Bar graph of fluorescence anisotropy of IKVAV PA solutions. Error bars correspond to three independent experiments. n.s., not significant; ***P < 0.0001; one-way ANOVA with Bonferroni. (B) (Top) Chemical structure of the IKVAV peptide sequence, highlighting the K residue probed by NMR. (Bottom) Bar graph of the K relaxation time for the different IKVAV PAs investigated. Error bars correspond to three runs per condition. ***P < 0.0001 versus IKVAV PA1; *P < 0.05, ***P < 0.0001 versus IKVAV PA5; one-way ANOVA with Bonferroni. (C) Differentiation conditions used for hNPCs. DMEM, Dulbecco's minimum essential medium. (D) Representative micrographs of hNPCs treated with IKVAV PA1, PA2, PA4, and PA5. NESTIN indicates the stem cells in red, ITGB1 indicates the receptors in green, and 4',6-diamidino-2-

phenylindole (DAPI) indicates the nuclei in blue. (**E**) WB results of ITGB1, p-FAK, FAK, ILK, and TUJ-1 in hNPCs treated with laminin (Lam) and the various IKVAV PAs. (**F**) Representative confocal micrographs of hNPCs treated with IKVAV PA1, PA2, PA4, and PA5. NESTIN indicates stem cells (red), SOX-2 indicates stem cells (green), TUJ-1 indicates neurons (white), and DAPI indicates nuclei (blue). (**G** and **H**) Bar graphs of the percentage of SOX-2⁺ and NESTIN⁺ stem cells (**G**) and TUJ-1⁺ neuronal cells (H) treated with the various IKVAV PAs. Error bars correspond to three independent differentiations. **P < 0.01, ***P < 0.001 versus IKVAV PA2 and **P < 0.01, ***P < 0.001 versus IKVAV PA5; one-way ANOVA with Bonferroni. (**I**) Fluorescence anisotropy (left) and K residue relaxation times (right) obtained for IKVAV PA2 nanofibers in the absence (no Ca²⁺) or presence (Ca²⁺) of calcium ions. ***P < 0.001; Student's P test. (**J**) WB results of ITGB1, p-FAK, FAK, and ILK in hNPCs treated with IKVAV PA2 in the absence (–) or presence (+) of Ca²⁺. Scale bars, 10 μm (D) and 100 μm (F).

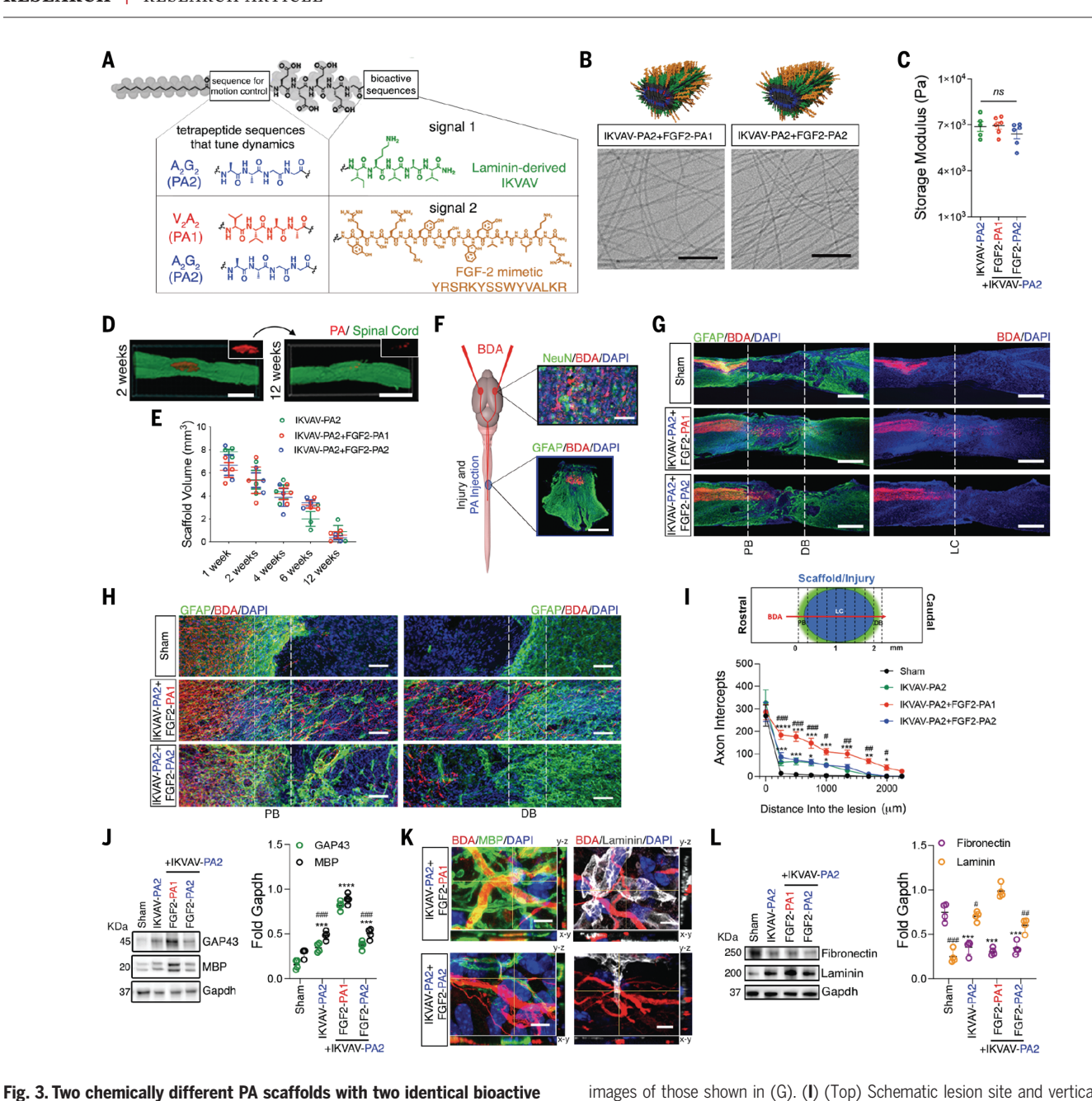
puromycin-based protein synthesis analysis [the surface sensing of translation (SUnSET) technique], we verified that all of the conditions showed similar protein translation levels, so the observed differences were not linked to a metabolic effect (fig. S16).

We also performed in vitro experiments in which hNPCs were treated with the most bioactive IKVAV PAs (PA2 and PA5) mixed with 5 mM CaCl₂, which is known to electrostatically cross-link negatively charged PA fibers (18, 19). The addition of Ca²⁺ suppressed supramolecular motion, which was confirmed by FD and T2-NMR experiments (Fig. 2I and fig. S17). When supramolecular motion was decreased

by adding Ca²⁺ ions to the media, the activation of ITGB1 and its downstream intracellular pathway (ILK and p-FAK-FAK) also decreased (Fig. 2J and fig. S18). These results showed a strong positive correlation between dynamics and in vitro bioactivity, as mutations were introduced in the tetrapeptide amino acid sequence in the nonbioactive domain of IKVAV PAs.

SCI model: Axon regrowth and formation of glial scar

We then proceeded to test the ability of dualsignal fibrils to enhance functional recovery after SCI in vivo. Given the low level of in vitro bioactivity observed for IKVAV PA1, PA3, PA4, PA6, PA7, and PA8, we did not to use these PAs in combination with the FGF2 PAs. We also needed nanofibers that display both signals simultaneously, so the binary systems had to be miscible and form hydrogels with similar mechanical properties upon contact with physiological fluids once injected at the site of the injury. Only IKVAV PA2 was both miscible and could form hydrogels with similar mechanical properties when mixed with either FGF2 PA1 or FGF2 PA2, particularly at a molar ratio of 90:10 (Fig. 3, A to C; fig. S19; and table S3). Furthermore, both FGF2 PAs alone formed highly aggregated short fibers that further contributed



(A) Chemical structures of the two PA molecules used. (B) (Top) Molecular graphics representation of a supramolecular nanofiber displaying two bioactive signals. (Bottom) Cryo-TEM micrographs of IKVAV PA2 coassembled with FGF2 PAs (FGF2 PA1 and FGF2 PA2). (C) Storage modulus of IKVAV PA2 (green) and their respective coassemblies with FGF2 PAs (FGF2 PA1, red; FGF2 PA2, blue). (D) Fluorescent micrographs of spinal cords (green) injected with IKVAV PA2 + FGF2 PA1 (red) covalently labeled with Alexa 647. (E) Dot plot of PA scaffold volume as a function of time after implantation. (F) (Left) Schematic illustration showing the site of BDA and PA injections. (Right) Fluorescent micrographs of the brain cortex (top)—stained for NeuN, neurons (green); BDA, labeled neurons (red); and DAPI, nuclei (blue)—and transverse spinal cord section (bottom)—stained for GFAP, astrocytes (green); BDA, labeled descending axons (red); and DAPI, nuclei

(blue). (G) Fluorescent micrographs of longitudinal spinal cord sections in sham, IKVAV PA2 + FGF2 PA1, and IKVAV PA2 + FGF2 PA2 groups. GFAP indicates

astrocytes (green), BDA indicates labeled axons (red), and DAPI indicates nuclei

border (DB), and the central part of the lesion (LC). (H) Representative magnified

(blue); vertical white dashed lines indicate the proximal border (PB), the distal

sequences reveal differences in growth of corticospinal axons after SCI.

images of those shown in (G). (I) (Top) Schematic lesion site and vertical lines used to count the number of axons crossing at each location indicated. (Bottom) Plot of the number of crossing axons. Error bars correspond to six animals per group. *P < 0.05, **P < 0.01, ***P < 0.001 versus sham and *P < 0.05, $^{\#}P < 0.01$. $^{\#\#}P < 0.001$ versus IKVAV PA2 and IKVAV PA2 + FGF2 PA2 groups: repeated measures of two-way ANOVA with Bonferroni, (J) WB results (left) and dot plot of the normalized values for GAP43 and MBP protein in sham, IKVAV PA2, IKVAV PA2 + FGF2 PA1, and IKVAV PA2 + FGF2 PA2 (right). **P < 0.01, ***P < 0.001 versus sham and ***P < 0.001 versus IKVAV PA2 + FGF2 PA1 group; one-way ANOVA with Bonferroni. (K) Representative three-dimensional fluorescent micrographs of BDA-labeled axon regrowth (red) and myelin basic protein (MBP) (green) (left) and laminin (white) (right). (L) WB results (left) and dot plot of the normalized values for laminin and fibronectin expression in conditions described in (J) (right). ***P < 0.001 versus sham and $^{\#}P$ < 0.05, $^{\#\#}P < 0.01, ^{\#\#\#}P < 0.001$ versus IKVAV PA2 + FGF2 PA1 group; one-way ANOVA with Bonferroni. Gapdh, glyceraldehyde-3-phosphate dehydrogenase. Data points in (E) correspond to three animals per group and to four animals per group in (J) and (L). Scale bars, 1500 μm [(D) and (G)], 25 μm [(F) top], 200 μm [(F) bottom], 100 μ m (H), and 2 μ m (K).

to immiscibility with other IKVAV PAs, such as PA1, PA4, or PA5 (figs. S20 and S21).

The miscible and gel-forming binary systems with similar mechanical properties-IKVAV PA2 with either FGF2 PA1 or FGF2 PA2-were taken forward to in vivo experiments (Fig. 3A and fig. S22; for full characterization of these systems, see supplementary text). We injected saline solutions of 90:10 molar ratio of IKVAV PA2 coassembled with either FGF2 PA1 or with FGF2 PA2 into the spinal cord of mice 24 hours after a severe contusion in an established murine model of SCI (see supporting information for specific details of the animal model protocol) (20). IKVAV PA2, which was the most bioactive single signal system, was used as a control in all in vivo experiments. All PA solutions gelled in situ when delivered into the spinal cord and localized into the damaged area. To track and quantify the bioactive scaffold's biodegradation as a function of time, the PA molecules were fluorescently labeled with Alexa 647 dye. We then injected the fluorescent materials into the spinal cord 24 hours after injury and measured their volume at 1, 2, 4, 6, and 12 weeks by fully reconstructing spinal cords using spinning disk confocal microscopy (Fig. 3D and supplementary materials). The soft materials biodegraded gradually within a period of 1 to 12 weeks after implantation, and we did not observe any differences in biodegradation rate among the three experimental materials (Fig. 3E and fig. S23).

We performed bilateral injections of biotinylated dextran amine (BDA) administered 10 weeks after the injury into the sensorimotor cortex to trace the corticospinal tracts (CSTs), which mediate voluntary motor function (Fig. 3F) (2I). We evaluated anterogradely labeled CST axon regrowth 12 weeks after injury in all PA and sham (injected with saline solution only) groups. This process required quantification of the number of labeled axons that regrew to the proximal lesion border and beyond. We also injected IKVAV PA1 and PA fibers lacking any bioactive signals on their surfaces (backbone PA) as controls (see fig. S24 and table S1 for the peptide sequence).

In mice injected with saline solution, we hardly observed any regrown axons within the lesion, whereas we observed some regrowth of axons for IKVAV PA1, in which fibers exhibited low mobility (Fig. 3G and fig. S25; see supplementary text for additional PA controls). By contrast, in mice injected with IKVAV PA2 alone or coassembled with FGF2 PA2 (which shares the same A_2G_2 nonbioactive domain as that in IKVAV PA2), we only observed a modest but increased axon regrowth compared with that seen in the sham condition. However, injections of IKVAV PA2 coassembled with FGF2 PA1 (which includes the V_2A_2 nonbioactive domain instead of A_2G_2) led to robust

corticospinal axon regrowth across the lesion site, even surpassing its distal border (Fig. 3, G and H, and fig. S26). In this group, the total axon regrowth within the lesion was twofold greater than that in the group using the coassembly of IKVAV PA2 and FGF2 PA2 and 50-fold greater than in the sham group (Fig. 31). Serotonin axons (5HT), which may also play a role in locomotor function, also regrew within the lesion core with a similar trend as that observed with CST (fig. S27).

We hypothesize that the CST and 5HT axon regrowth observed could be in part the result of the absence of a substantial astrocytic scar, which is a strong barrier for axonal regeneration (11). In the sham and backbone PA groups. this barrier was revealed as a dense population of reactive astrocytes expressing high levels of glial fibrillary acidic protein (GFAP) at the borders of the injury, whereas in all bioactive PA groups, the glial scar was less dense (Fig. 3H and figs. S25 and S26). In agreement with these results, WB analysis showed a higher level of growth-associated protein 43 (GAP-43), which resides in the growth cone of regenerating axons, only in the most bioactive coassembly (IKVAV PA2 + FGF2 PA1) (Fig. 3J).

Finally, we determined whether PA scaffolds could induce remyelination of corticospinal axons 3 months after injury and found high levels of myelin basic protein (MBP) within the lesion, particularly wrapping the regrown axons in IKVAV PA2 + FGF2 PA1 (Fig. 3, J and K). Moreover, in this condition, we observed many growing axons within the lesion to be in contact with high levels of laminin and low levels of fibronectin, indicative of a reduced fibrotic core (Fig. 3, K and L, and fig. S26). Our histological and biochemical observations suggested that physical differences between the two supramolecular coassemblies bearing two bioactive signals could greatly enhance neuroregenerative outcomes after injury.

SCI model: Angiogenesis, cell survival, and functional recovery

We next explored the effect of both dual-signal coassemblies on angiogenesis at the site of injury, which is important for a fully anatomical and functional regeneration. Relative to uninjured tissue sections, the transverse spinal cord sections of sham mice revealed a substantial degree of tissue degeneration extending rostro-caudally >2.0 mm away from the center of the lesion. In this case, a significant decrease in vascular area fraction, vascular length, and branching was observed compared with that observed in the uninjured control (Fig. 4, A and B). We assessed the existence of a functional vessel network by transcardially injecting a glucose solution containing 1,1'-dioctadecyl-3,3,3',3'-tetramethylindocarbocyanine perchlorate (DiI), a lipophilic carbocyanine dye that incorporates into endothelial cell membranes (Fig. 4A) (22). In groups treated with PA scaffolds, there was high preservation of the ventral tissue structure, revealing the maintenance of a functional blood vessel network. However, we again observed that treatment with the most bioactive coassembly led to an increase in vascular area fraction, vascular length, and branching, especially in the dorsal region (Fig. 4, A and B, and fig. S28). These parameters did not differ significantly between the IKVAV PA2 alone and the less bioactive coassembly group (IKVAV PA2 + FGF2 PA2), which implies that the mimetic FGF2 angiogenic signal was not functioning optimally in IKVAV PA2 + FGF2 PA2.

To determine the origin of the blood vessels within the lesion, the thymidine analog 5'-bromo-2'-deoxyuridine (BrdU) was intraperitoneally injected during the first week after injury, and we observed newly formed blood vessels within the lesion of the most bioactive coassembly group 12 weeks after injury. This was confirmed by a significant increase in the number of double positive BrdU⁺ and CD31⁺ cells relative to samples for all other groups (Fig. 4, C and D, and fig. S29) as well as by WB analysis (Fig. 4E). The IKVAV PA2 + FGF2 PA2 coassembly and IKVAV PA2 alone led to a very modest but significantly increased blood vessel formation compared with that observed in the sham group.

We also assessed the effect of both dualsignal coassemblies on neuronal survival, maintenance of spinal circuitry, and local function. Native FGF-2 has previously been associated with an increase in neuronal viability after SCI (23). Transverse spinal cord sections of the most bioactive coassembly group showed NeuN⁺ neurons near the newly generated vessels in the dorsal region similar to the uninjured control group (Fig. 5A). Furthermore, neurons (NeuN+ cells) that were also ChAT+ (motor neurons) were only found in the ventral horn when PAs were utilized, showing a significantly higher number in the most bioactive system relative to other groups (Fig. 5, B and C). The lack of any double positive BrdU⁺ and NeuN⁺ neurons within the lesion in any of the groups suggested the absence of local neurogenesis.

We investigated whether the observed axonal regeneration, angiogenesis, and local neuronal cell survival led to behavioral improvement in injured animals. For this purpose, we obtained Basso mouse scale (BMS) open field locomotor scores and locomotor recovery by footprint analysis in all groups during the 12 weeks after injury (Fig. 5D and fig. S30). At 1 week after injury and thereafter, all PA groups demonstrated significant and sustained behavioral improvement compared with that of the sham group. Notably, 3 weeks after

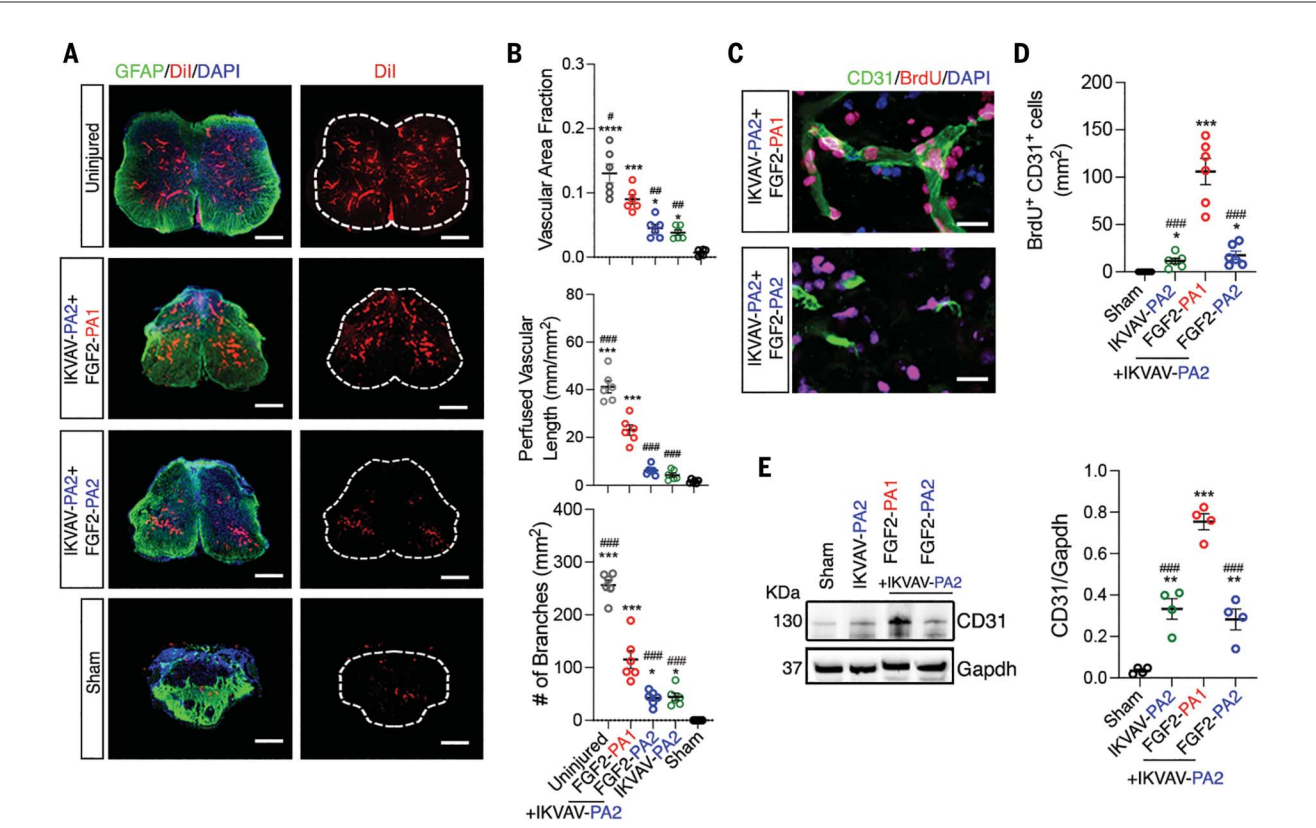


Fig. 4. Two chemically different PA scaffolds with two identical bioactive sequences reveal differences in angiogenesis. (**A**) Fluorescent micrographs of transverse spinal cord sections in uninjured, IKVAV PA2 + FGF2 PA1, IKVAV PA2 + FGF2 PA2, and sham groups. GFAP indicates astrocytes (green), Dil indicates labeled blood vessels (red), and DAPI indicates nuclei (blue). (**B**) Dot plots of the vascular area fraction, perfused vascular length, and number of branches in the transverse sections of groups in (A). *P < 0.05, ***P < 0.0001 versus sham and *P < 0.001, *P < 0.001,

FGF2 PA2. CD31 indicates blood vessels (green), BrdU indicates newly generated cells (red), and DAPI indicates nuclei (blue). (**D**) Dot plot of the number of BrdU⁺ and CD31⁺ cells per square millimeter in groups treated with IKVAV PA2 alone, IKVAV PA2 + FGF2 PA1, IKVAV PA2 + FGF2 PA2, and saline (sham). *P < 0.05, ***P < 0.001 versus sham and **#*P < 0.0001 versus IKVAV PA2 + FGF2 PA1 group; one-way ANOVA with Bonferroni. (**E**) WB results (left) and dot plot of the normalized values for CD31 protein (right). **P < 0.001, ***P < 0.0001 versus sham and **#*P < 0.001 versus IKVAV PA2 + FGF2 PA1 group; one-way ANOVA with Bonferroni. Data points in (B) and (D) correspond to six animals per group and to four animals per group in (E). Scale bars, 200 μm (A) and 25 μm (C).

injury, mice treated with the most bioactive coassembly showed a significant functional recovery (5.9 \pm 0.5) compared with that observed in mice injected with IKVAV PA2 + FGF2 PA2 and IKVAV PA2 alone (4.4 ± 0.5) and 4.3 ± 0.5 , respectively) (Fig. 5D). Quantification of footprints revealed significantly larger stride lengths and widths in mice treated with the most bioactive coassembly relative to those of other groups (fig. S30). Collectively, these data suggest that the neuronal cell survival and functional recovery that we observed in dual-signal systems are unexpectedly linked to the differences in the chemical composition of their respective nonbioactive tetrapeptides.

In vitro results on human endothelial and neural progenitor cells

On the basis of the results described above, we next investigated the bioactivity of the FGF2 signal in vitro in both coassemblies using human umbilical vein vascular endothelial cells (HUVECs). As mentioned previously, native FGF-2 enhances endothelial cell proliferation and network formation (24), and we found that within 48 hours of culturing HUVECs on the most bioactive coassembly or FGF2 protein, there was extensive branching and formation of vessel-like capillary networks (Fig. 6, A and B, and fig. S31; see also supplementary materials for methodology used). We also performed WB analysis to verify whether the observed in vitro bioactivity of the FGF2 PA1 coassembled with the IKVAV PA2 was linked to the FGF-2 intracellular signaling pathway. HUVECs treated with the most bioactive coassembly or native FGF-2 revealed high levels of p-FGFR1 and the downstream proteins phospho-extracellular signal-regulated kinase 1 (p-ERK1) and p-ERK2 (p-ERK1/2), which activate the proliferation and migration of endothelial cells (Fig. 6C) (6, 25). As expected, systems containing the scrambled FGF2 mimetic sequence did not reveal any bioactivity (figs. S31 and S32).

To establish the simultaneous bioactivity of the IKVAV and FGF2 signals in both coassemblies, we assessed the effects of these molecules on hNPC proliferation in vitro by quantifying the double positive EdU^+ and $SOX-2^+$ as well as the induction of ITGB1 and p-FGFR1 (Fig. 6, D to F, and fig. S33; see also supplementary text for more information). These experiments suggest that the FGF2 signal in the less bioactive coassembly is largely nonfunctional, whereas the IKVAV signal remains operative in both. These results are consistent with our observations in the SCI experiments.

Physical experiments and computer simulations on supramolecular motion

We investigated what might be the physical reasons for the loss of in vitro and in vivo bioactivity when the tetrapeptide that follows the

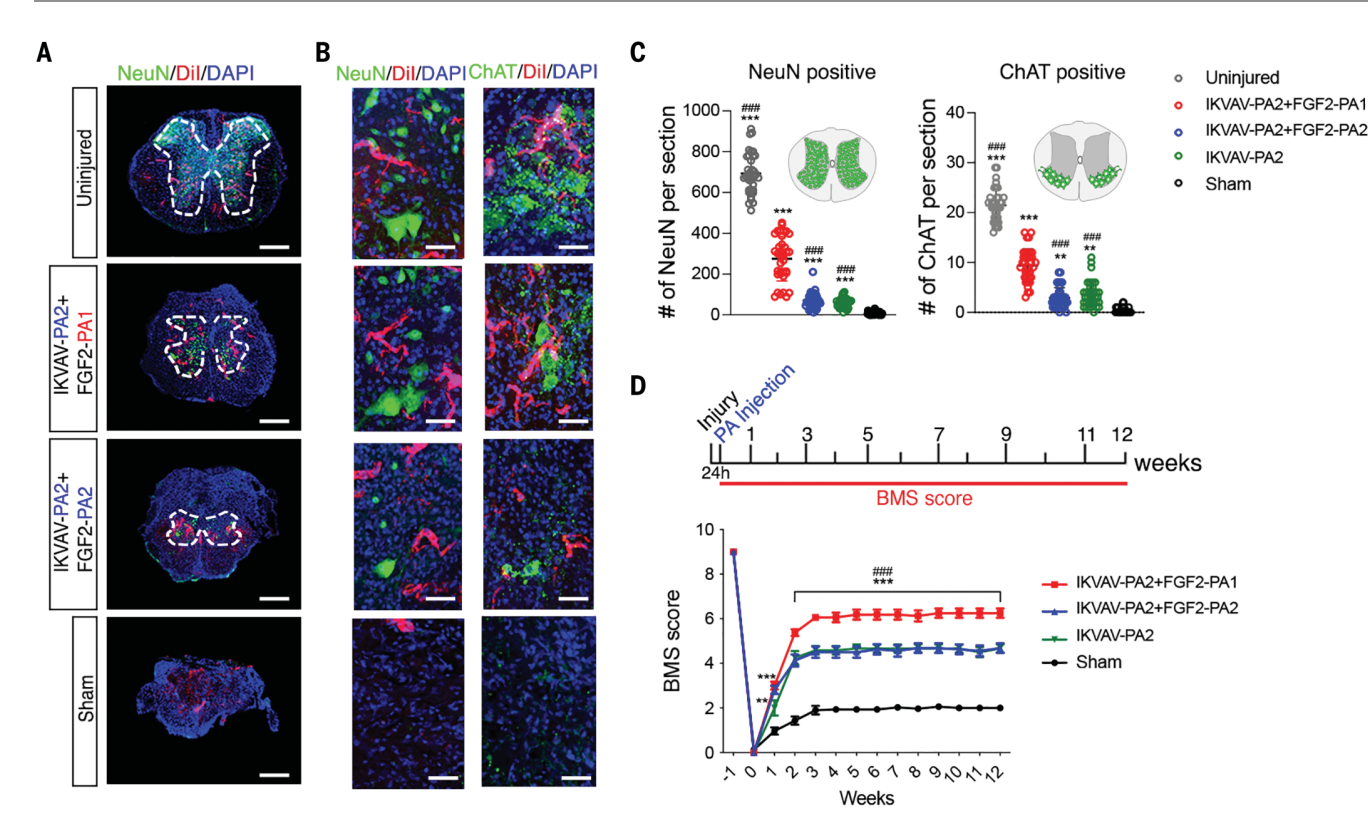


Fig. 5. Two chemically different PA scaffolds with two identical bioactive sequences reveal differences in neuronal survival and functional recovery.

(A) Fluorescent micrographs of transverse spinal cord sections corresponding to uninjured, IKVAV PA2 + FGF2 PA1, IKVAV PA2 + FGF2 PA2, and sham groups. NeuN indicates neurons (green), Dil indicates labeled blood vessels (red), and DAPI indicates nuclei (blue); dashed lines indicate the gray matter (horn).

(B) High-magnification images of the ventral horn area for slices in (A). On the left, NeuN indicates neurons (green), Dil indicates labeled blood vessels (red), and DAPI indicates nuclei (blue); on the right, ChAT indicates motor neurons (green), Dil indicates labeled blood vessels (red), and DAPI indicates labeled blood vessels (red), and DAPI indicates

nuclei (blue). **(C)** Dot plots showing the number of NeuN⁺ (left) and ChAT⁺ (right) cells per transverse section. Data points correspond to a total of 48 sections; eight sections per animal and six animals per group. **P < 0.01, ***P < 0.001 versus sham and ***P < 0.001 versus IKVAV PA2 + FGF2 PA1 group; one-way ANOVA with Bonferroni. **(D)** Experimental time line of in vivo experiments (top) and BMS for locomotion (bottom). Error bars correspond to 38 animals per group. **P < 0.001, ***P < 0.0001 all PA groups versus sham and ***P < 0.0001 versus IKVAV PA2 + FGF2 PA2 and IKVAV PA2 groups; repeated measures of two-way ANOVA with Bonferroni. Scale bars, 200 µm (A) and 20 µm (B).

alkyl tail was mutated from V₂A₂ to A₂G₂ in the FGF2 PAs. Differences in dynamics between FGF2 PA molecules in the two coassemblies were studied with T2-NMR spectroscopy and FD (Fig. 6, G to I). We measured the relaxation rates of the aromatic protons in Y and W amino acids, which are only present in the FGF2 mimetic signal (26, 27). The rates were slower in the most bioactive coassembly, indicating greater supramolecular motion in the signaling peptide (${}^{1}\text{H-R}_{2} = 49.3 \pm 11 \text{ s}^{-1} \text{ versus}$ $80.9 \pm 18.9 \text{ s}^{-1}$ for the less bioactive coassembly) (Fig. 6, G and H, and fig. S34). We also carried out FD experiments on the two coassemblies using FGF2 PA molecules that were covalently labeled with a Cy3 dye (based on cryo-TEM images, the dye did not disrupt the supramolecular assemblies; fig. S35). A lower anisotropy was found in the most bioactive coassembly, indicating a higher mobility of the FGF2 signal molecules within the nanofibers (Fig. 6I).

CG-MD simulations supported the T2-NMR and FD results above by yielding higher RMSF values for FGF2 PA molecules in the most bioactive coassembly. The simulations also revealed that FGF2 PA molecules form clusters in both coassemblies (slightly larger in the most bioactive system) with a distribution of mobilities (RMSF values) (Fig. 6J, fig. S36, and supplementary materials). The decrease in bioactivity in one of the systems could be attributed to differences in the extent of coassembly between the two PA molecules bearing signals. However, one-dimensional proton nuclear magnetic resonance (1D ¹H-NMR), diffusion ordered spectroscopy (DOSY), and T2-NMR (28, 29) of methylene units in alkyl tails indicate the occurrence of coassembly in both systems (figs. S37 to S39, table S4, and supplementary text).

The results obtained on greater degrees of motion in FGF2 PA1 molecules were counterintuitive because the tetrapeptide V_2A_2

(present in FGF2 PA1) had the least mobility in systems containing only IKVAV PA. The lower mobility in FGF2 PA2 molecules in the coassembly with IKVAV PA2 was likely the result of greater interactions through hydrogen bonding and side chain contacts among the identical tetrapeptides present in both molecules. By contrast, two dissimilar tetrapeptides are present in the two molecules of the highly bioactive IKVAV PA2 + FGF2 PA1 coassembly, which would not favor a strong interaction between both types of molecules and lead to higher degrees of supramolecular motion.

The evidence for a strong interaction between IKVAV PA2 and FGF2 PA2 and less motion is the essentially invariant circular dichroism (CD) spectrum when FGF2 PA2 is added to IKVAV PA2. However, the CD spectrum was modified when the less interactive FGF2 PA1 was added to IKVAV PA2, suggesting a disruption of secondary structure (fig. S40).

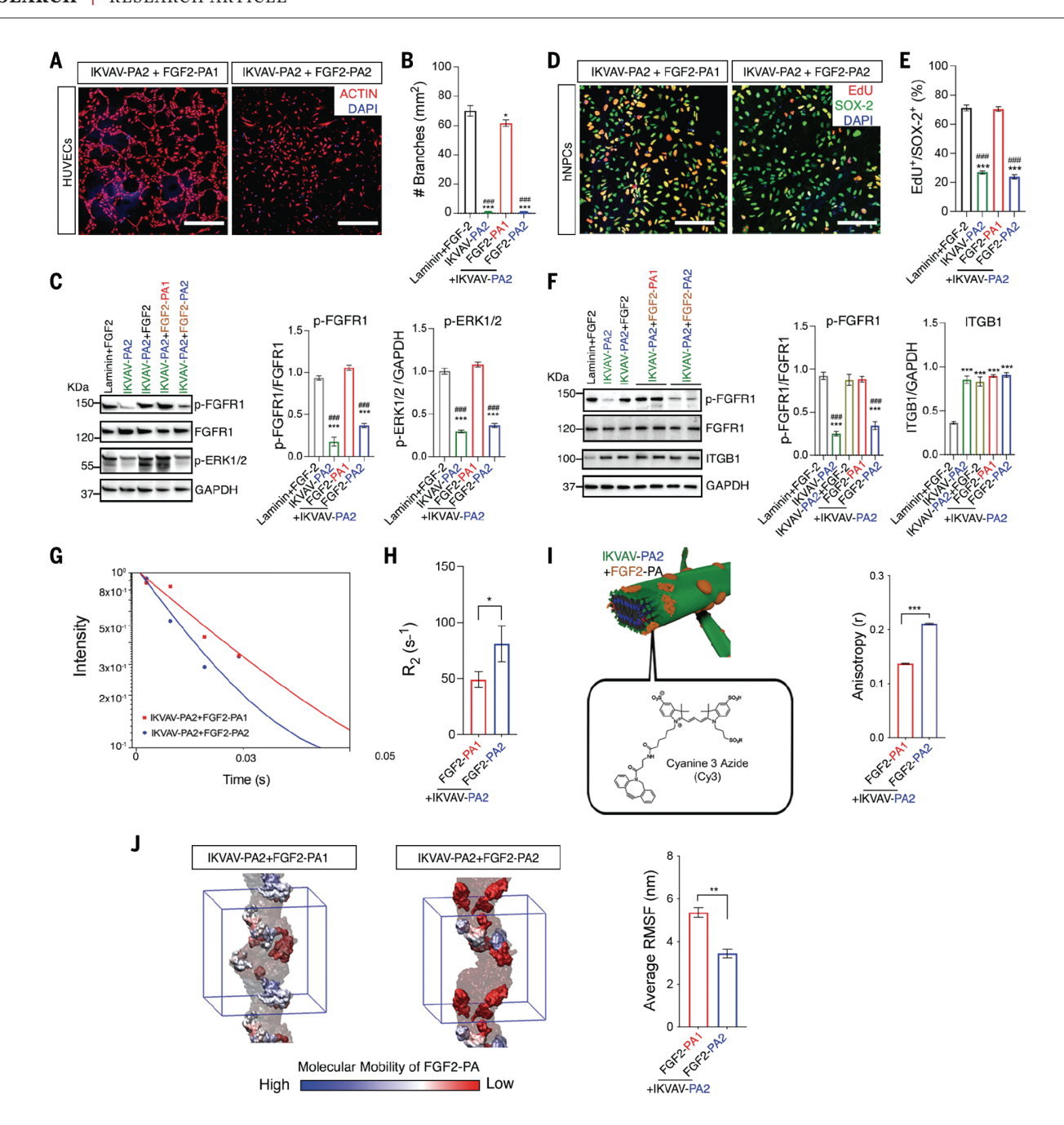


Fig. 6. Validating cell-signaling differences in vitro between two PA scaffolds exhibiting different supramolecular motion. (A) Confocal micrographs of HUVECs treated with IKVAV PA2 + FGF2 PA1 and IKVAV PA2 + FGF2 PA2. ACTIN indicates cytoskeleton (red) and DAPI indicates nuclei (blue). (B) Bar graph of the number of branches in HUVECs treated with laminin + FGF-2, IKVAV PA2 alone, IKVAV PA2 + FGF2 PA1, and IKVAV PA2 + FGF2 PA2. (C) WB results (left) and bar graphs of the normalized values for active FGFR1 (p-FGFR1) versus total FGFR1 (FGFR1) and active ERK1/2 (p-ERK1/2) using the conditions in (B) (right). (D) Confocal micrographs of hNPCs on coatings of IKVAV PA2 + FGF2 PA1 and IKVAV PA2 + FGF2 PA2. EDU indicates proliferative marker (red), SOX-2 indicates neural stem cell marker (green), and DAPI indicates nuclei (blue). (E) Bar graph of the percentage of EDU⁺ and SOX-2⁺ cells on the various coatings. (F) WB results (left) and bar graphs of the normalized values for active FGFR1 (p-FGFR1) versus total FGFR1 (FGFR1) and β1-INTEGRIN (ITGB1) (right). (G) ¹H-NMR spin-spin relaxation time of the

aromatic protons in Y and W amino acids in the FGF2 mimetic signal at 6.81 ppm (solid lines are single linear best fits). **(H)** Bar graph of the aromatic relaxation times measured in (G). Error bars correspond to three runs per condition. *P < 0.05; Student's t test. **(I)** Bar graph of fluorescence anisotropy of FGF2 PAs chemically modified with Cy3 dye. Error bars correspond to three independent experiments. ***P < 0.001; Student's t test. **(J)** Color-coded representation of RMSF values in clusters of FGF2 PAs (left) and the corresponding bar graph (right). IKVAV PA2 molecules are shown in transparent gray, ions and water molecules are removed for clarity, and the simulation box is shown in blue. Error bars correspond to five independent simulations. ***P < 0.01; Student's t test. Error bars in (B) and (E) correspond to three independent experiments and in (C) and (F) correspond to four independent experiments per condition. ***P < 0.0001 versus laminin + FGF2 and *##P < 0.0001 versus IKVAV PA2 + FGF2 PA1; one-way ANOVA with Bonferroni. Scale bars, 200 μ m (A) and 100 μ m (D).

Thus, the greater motion detected by NMR for FGF2 PA1 molecules must indicate freer translational motion of its clusters within the fibrils or vertical motion of the signaling clusters in and out of the fibrils. Although we have gathered substantial evidence for the correlation between supramolecular motion and bioactivity of fibrillar scaffolds used here to promote SCI recovery, we could not directly link this physical phenomenon to our in vivo observations with techniques currently available.

Discussion

Our work demonstrates that bioactive scaffolds that physically and computationally reveal greater supramolecular motion lead to greater functional recovery from SCI in the murine model. In one-dimensional scaffolds of noncovalently polymerized bioactive molecules, we expected polyvalency effects to help cluster receptors for effective signaling. We also expected that the internal structure of the supramolecular scaffolds could limit free motion and favorably orient signals toward receptors perpendicular to their fibrillar axis. However, the unexpected finding in this work is that the intensity of molecular motions within the bioactive fibrils, as measured on the bench, correlated with enhanced axonal regrowth, neuronal survival, blood vessel regeneration, and functional recovery from SCI. A direct link between the motion and the recovery will require techniques not currently available that could precisely detect supramolecular motion in vivo with high resolution.

However, the computer simulations and experimental data do suggest that translation on the scale of nanometers within or vertically out of the assemblies to reach receptor sites might enhance bioactivity. That is, a highly agile and physically plastic supramolecular scaffold could be more effective at signaling receptors in cell membranes undergoing rapid shape fluctuations. An alternative hypothesis for the cause of the recovery could be broadly more-favorable interactions of the molecularly dynamic scaffolds with the protein milieu of the ECM. In the context of our correlative findings between supramolecular motion and bioactivity, it is intriguing to ask why there is such a prevalence of intrinsically disordered proteins in biological systems (30), and one wonders whether the added motion of disordered protein domains, in analogy to our bioactive and dynamic supramolecular fibrils, provides greater capacity to signal efficiently in the biological environment. We conclude that our observations suggest great opportunities in the structural design of dynamics to optimize the bioactivity of therapeutic supramolecular polymers.

REFERENCES AND NOTES

- 1. G. A. Silva et al., Science 303, 1352-1355 (2004).
- D. E. Discher, D. J. Mooney, P. W. Zandstra, Science 324, 1673–1677 (2009).
- B. K. Brandley, R. L. Schnaar, Anal. Biochem. 172, 270–278 (1988).
- J. D. Hartgerink, E. Beniash, S. I. Stupp, Science 294, 1684–1688 (2001).
- T. Aida, E. W. Meijer, S. I. Stupp, Science 335, 813–817 (2012).
- C. M. Rubert Pérez, Z. Álvarez, F. Chen, T. Aytun, S. I. Stupp, ACS Biomater. Sci. Eng. 3, 2166–2175 (2017).
- V. M. Tysseling-Mattiace et al., J. Neurosci. 28, 3814–3823 (2008).
- S. Sur, C. J. Newcomb, M. J. Webber, S. I. Stupp, *Biomaterials* 34, 4749–4757 (2013).
-). J. H. Ortony et al., Nat. Mater. 13, 812–816 (2014).
- 10. C. S. Ahuja et al., Nat. Rev. Dis. Primers **3**, 17018 (2017).
- A. P. Tran, P. M. Warren, J. Silver, *Physiol. Rev.* 98, 881–917 (2018).
- J. E. Goldberger, E. J. Berns, R. Bitton, C. J. Newcomb, S. I. Stupp, Angew. Chem. Int. Ed. 50, 6292–6295 (2011).
- O.-S. Lee, V. Cho, G. C. Schatz, Nano Lett. 12, 4907–4913 (2012).
- A. N. Edelbrock et al., Nano Lett. 18, 6237–6247 (2018).
- L. Yap, H. G. Tay, M. T. X. Nguyen, M. S. Tjin, K. Tryggvason, Trends Cell Biol. 29, 987–1000 (2019).
- 16. L. Pan et al., PLOS ONE 9, e104335 (2014).
- 17. W. L. Lei et al., Cell Res. 22, 954-972 (2012).
- J. C. Stendahl, M. S. Rao, M. O. Guler, S. I. Stupp, Adv. Funct. Mater. 16, 499–508 (2006).
- M. A. Greenfield, J. R. Hoffman, M. O. de la Cruz, S. I. Stupp, *Langmuir* 26, 3641–3647 (2010).
- O. G. Bhalala, L. Pan, H. North, T. McGuire, J. A. Kessler, Bio. Protoc. 3, e866 (2013).
- 21. M. A. Anderson *et al.*, *Nature* **561**, 396–400 (2018).
- 22. Y. Li et al., Nat. Protoc. 3, 1703-1708 (2008).
- 23. M. Kasai, T. Jikoh, H. Fukumitsu, S. Furukawa, *J. Neurotrauma* **31**, 1584–1598 (2014).
- M. Murakami, T. Sakurai, WIREs Syst. Biol. Med. 4, 615–629 (2012).
- R. Goetz, M. Mohammadi, *Nat. Rev. Mol. Cell Biol.* 14, 166–180 (2013).
- 26. D. F. Gauto et al., J. Am. Chem. Soc. **141**, 11183–11195 (2019).
- 27. Y. Toyama et al., Nat. Commun. 8, 14523 (2017).
- K. H. Gardner, L. E. Kay, Annu. Rev. Biophys. Biomol. Struct. 27, 357–406 (1998).
- 29. M. Kainosho et al., Nature 440, 52-57 (2006).
- P. E. Wright, H. J. Dyson, *Nat. Rev. Mol. Cell Biol.* 16, 18–29 (2015).

The authors are grateful to M. Karver, E. Testa, and S. Biswas

of the Peptide Synthesis Core Facility of the Simpson Ouerrey

ACKNOWLEDGMENTS

Institute for BioNanotechnology at Northwestern University for their assistance and key insights into the synthesis and purification of the PAs. We also thank the laboratory of J. A. Kessler for the initial training of Z.A., A.N.K.-E., and F.C. on the SCI model. We thank M. Seniw for the preparation of graphic illustrations shown in the figures. The authors would also like to thank C. Rubert-Perez, L. C. Palmer, and K. Sato for their initial help with the FGF2 PA materials, especially for helpful discussions about materials characterization and CD results. Funding: The experimental work and simulations were supported by the Louis A. Simpson and Kimberly K. Ouerrey Center for Regenerative Nanomedicine at the Simpson Querrev Institute for BioNanotechnology (S.I.S.). Work on NMR analysis was supported by the Air Force Research Laboratory under agreement no. FA8650-15-2-5518. Part of the biological experiments reported here was supported by the National Institute on Neurological Disorders and Stroke (NINDS) and the National Institute on Aging (NIA) R01NS104219 (E.K.), NIH/ NINDS grants R21NS107761 and R21NS107761-01A1 (E.K.), the

Les Turner ALS Foundation (E.K.), and the New York Stem Cell Foundation (E.K.). We thank the Paralyzed Veterans of America (PVA) Research Foundation PVA17RF0008 (7 A.), the National Science Foundation (A.N.K.-E. and S.M.C.), and the French Muscular Dystrophy Association (J.A.O.) for graduate and postdoctoral fellowships. We thank the Peptide Synthesis Core and the Analytical Bionanotechnology Equipment Core at the Simpson Querrey Institute for Bionanotechnology for biological and chemical analyses. These facilities have support from the Soft and Hybrid Nanotechnology Experimental (SHyNE) Resource (NSF ECCS - 1542205). Imaging work was performed at the Center for Advanced Microscopy, and CD measurements were performed at the Northwestern University Keck Biophysics facility. Both of these facilities are generously supported by NCI CCSG P30 CA060553 awarded to the Robert H. Lurie Comprehensive Cancer Center. Spinning disk confocal microscopy was performed on an Andor XDI revolution microscope, purchased through the support of NCRR 1S10 RR031680-01. Multiphoton microscopy was performed on a Nikon A1R multiphoton microscope, acquired with support from NIH 1S100D010398-01. Tissue processing was performed at the Pathology Core Facility supported by NCI CA060553 awarded to the Robert H. Lurie Comprehensive Cancer Center. Electron microscopy experiments were performed at the Electron Probe Instrumentation Center (EPIC) and the BioCryo facility of Northwestern University's NUANCE Center, both of which have received support from the SHvNE Resource (NSF ECCS-1542205); the MRSEC program (NSF DMR-1720139) at the Materials Research Center; the International Institute for Nanotechnology (IIN); the Keck Foundation; and the State of Illinois, through the IIN. NMR and Fourier transform infrared spectroscopy characterization in this work made use of IMSERC at Northwestern University, which has received support from the SHyNE Resource (NSF ECCS-1542205), the State of Illinois, and IIN. Portions of this work were performed at the DuPont-Northwestern-Dow Collaborative Access Team (DND-CAT) located at Sector 5 of the Advanced Photon Source (APS). DND-CAT is supported by Northwestern University, The Dow Chemical Company, and DuPont de Nemours, Inc. This research used resources of the Advanced Photon Source, a US Department of Energy (DOE) Office of Science User Facility operated for the DOE Office of Science by Argonne National Laboratory under contract no. DE-ACO2-06CH11357. E.K. is a Les Turner ALS Research Center Investigator and a New York Stem Cell Foundation-Robertson Investigator. Authors contributions: Z.A. designed the materials, performed in vitro and in vivo experiments, analyzed data, and wrote the manuscript. A.N.K.-E. prepared all the materials, performed some of the materials characterization, and conducted in vivo experiments, I.R.S. performed some of the materials characterization, carried out the computational simulations, analyzed the simulated data, and took part in discussions, J.A.O. carried out hNPCs in vitro experiments and took part in discussions. R.Q. performed some of the materials characterization and analysis. Z.S. and P.A.M. carried out the NMR experiments and analyzed the data. F.C. assisted during the in vivo experiments. S.M.C. acquired cryo-TEM imaging. S.W. carried out experiments at Argonne National Laboratory. E.K. supervised hNPCs in vitro studies and took part in discussions. S.I.S. supervised the research and wrote the manuscript. All authors helped to edit and approved the final version of the manuscript. Competing interests: Z.A. and S.I.S. are inventors on a pending patent pertaining to this work (Supramolecular Motion in Bioactive Scaffolds Promotes Recovery from Spinal Cord Injury). The authors declare no other competing interests. Data and materials availability: All data needed to evaluate the conclusions in the paper are present either in the main text or the supplementary materials.

SUPPLEMENTARY MATERIALS

science.org/doi/10.1126/science.abh3602 Materials and Methods Supplementary Text Figs. S1 to S40 Tables S1 to S4 References (31–50)

3 March 2021; resubmitted 16 July 2021 Accepted 23 September 2021 10.1126/science.abh3602